Thin Frequency-Selective Lattices Integrated in Novel Compact MIC, MMIC, and PCA Architectures

Harry Contopanagos, *Member, IEEE,* Lijun Zhang, and Nicolaos G. Alexopoulos, *Fellow, IEEE*

***Abstract*—We analyze and optimize the design of novel composite materials for IC's and printed circuit antenna (PCA) applications. We are using a variety of finite artificial lattices (FAL's) carrying passive metalo-dielectric unit cells. We first examine and optimize these lattices as freestanding structures, regarding them as FSS's and space filters. We obtain several designs for appropriate metalo-dielectric unit cells, as well as stacking geometries for constructing thin laterally infinite artificial lattices. Further, we examine the action of the corresponding FAL within integrated architectures, emphasizing crosstalk suppression, circuit-coupling tailoring, and gain enhancement. We find very significant directive gain enhancements for compact packaged PCA applications. Finally, anomalous scaling of the resulting circuits and tunable designs are also presented.**

***Index Terms*—Finite-element methods, frequency-selective surfaces, integral equations, microstrip antennas, microwave integrated circuits, photonic bandgap materials, transfer matrix.**

I. Introduction

INCREASING integrated circuit (IC) density for new technologies meets severe limitations for high-frequency applications. The resulting electrical dimensions of the circuit components meet corresponding resonant frequencies within the operating bands, resulting in resonant crosstalk and highly dispersive behavior. To overcome these limitations, current designs require spreading out individual components in order to suppress strong coupling or, conversely, placing an upper limit on operating frequencies for a given packing density.

A very promising approach to overcome these limitations is to use novel artificial frequency-selective materials, preferably in thin-layered geometries, for the purpose of either eliminating crosstalk in certain frequency bands or tailor designing a certain response. For example, if the IC is a cavity-backed printed antenna, it may be desirable to use such materials in order to isolate antenna performance from its associated circuitry or unwanted cavity resonances or to use these materials as superstrates (covers) for protection. In this latter case, it is desirable to design the cover so that it enhances the radiation patterns of the antenna itself, rather than designing it to simply minimally interfere with antenna operation.

Photonic bandgap (PBG) materials [1] have recently attracted a lot of attention in the engineering community because they are natural candidates for such applications. These materials are composed of unit cells containing artificial implants embedded within a host dielectric and periodically placed to form an artificial crystal lattice in one, two, or three dimensions. The scattering response of the implants is intended to be very different than the surrounding dielectric host, creating significant electromagnetic interference between implant and host. This interference depends on both host and implant (design of unit cell) and crystal geometry. By appropriate design of these parameters, one can achieve large transmission suppressions in specific frequency bands (i.e., PBG's) and uninhibited transmission in other bands. As we will show, transmission characteristics are tailored not only in frequency, but also in incidence angle, which makes PBG materials ideal candidates for frequency-selective surfaces (FSS's) and space filters, as well as for IC substrates/superstrates where filtering response of particular modes (e.g., surface modes) is desired.

A fundamental classification of operating frequencies for a given PBG material regards its response as an effective medium or as a crystal.

A. Effective Medium Theory Limit

For wavelengths much longer than the characteristic electrical dimensions of the unit cell, the frequency response of a PBG depends on calculable effective permittivities and permeabilities and not on the specific geometry of the artificial crystal lattice. The effective bulk optical quantities of the material solely depend on the unit-cell structure and can be used in specific planar geometries within circuit and antenna applications. We stress here that this effective medium theory (EMT) limit is not devoid of interest since one can design unit cells providing highly dispersive refractive indexes, which strongly affect thin-film performance and filter response within given integrated architectures.

B. Strong Coupling Limit

For wavelengths comparable with the electrical dimensions of the unit cell, strong coupling and interference arises, EMT breaks down, and the full scattering problem must be solved

Manuscript received March 20, 1998; revised July 22, 1998. This work was supported in part by the U.S. Army Research Office under Contract DAAH04-96-1-0389.

H. Contopanagos and L. Zhang are with the Department of Electrical Engineering, University of California at Los Angeles, Los Angeles, CA 90095 USA (e-mail: contopan@ee.ucla.edu, lzhang@ee.ucla.edu).

N. G. Alexopoulos is with the Department of Electrical and Computer Engineering, University of California at Irvine, Irvine, CA 92697 USA (e-mail: alfios@uci.edu).

Publisher Item Identifier S 0018-9480(98)08340-9.

either numerically or through multipole expansions. It is in this region that the material response is strongly coupled with the surrounding circuit architecture *and at the same time* strongly depends on both the unit cell *and* artificial lattice comprising the material.

From these properties, it follows that conventional scaling laws for IC's may only hold approximately or not at all. Even within the EMT limit, the statement that a circuit response will essentially scale periodically with frequency as $k_0 \cdot w$, where k_0 is the free-space wavenumber and w a (uniform) length scale of the circuit, assumes constant (i.e., not dependent on either frequency or length scale) refractive indexes for the circuit substrates. Within the EMT limit for PBG materials used in the circuits, the PBG unit cell should be considered part of the circuit since it will be itself subject to design. Scattering off these materials will depend irreducibly on $\{n(k_0, w), n(k_0, w) \cdot k_0 \cdot w\}$, where $n(k_0, w)$ is the complex refractive index of the PBG material. For specific choices of unit cells, it is possible that n depends on the length scale w and, in some cases, on both k_0, w. Therefore, the scaling law may be anomalously affected even within EMT. For operation in the strong coupling limit, circuit characteristics will show a much stronger deviation from conventional scaling, which will not even be describable in terms of refractive indexes. For this situation, full-wave analysis of the circuits and their scaling properties is necessary.

The arrangement of this paper is as follows. In Section II, we present a generic analytical discussion of freestanding PBG materials focusing on metalo-dielectric unit cells. This class of unit cells is important because even though they are passive, they can be designed to have strong, direction-dependent, capacitive, and inductive interactions and operate as microelectromechanical (MEM) devices within the material. Our analytical approach provides a physical understanding of the effects of the design of the unit cell within the thin lattice geometry on the frequency selectivity. It also provides design directions, which we can further exploit with our finite-element integral-equation method (FE–IEM) code, and a first step in deducing circuit equivalents for PBG materials in the strong coupling limit for future use in high-speed low-memory coding. Finally, we illustrate our ideas about anomalous scaling at high frequencies and the possibility of *using such scaling advantageously* for given circuit densities.

In Section III, we present the structure of our new FE–IEM code for analyzing thin finite artificial lattices (FAL's) embedded within realistic circuits. This code can analyze laterally infinite periodic geometries *and* laterally finite arbitrary geometries. These are the two most useful classes for our purposes. However, the code cannot analyze laterally infinite (or electrically very large) arbitrary geometries.

In Section IV, we present analysis, design, and optimization of a variety of three-dimensional (3-D) freestanding FSS's. We especially focus on thin artificial crystals composed of a small number of two-dimensional (2-D) PBG layers stacked in an arbitrary scheme.

In Section V, we integrate some of these PBG designs within realistic laterally finite-circuit and printed-antenna architectures and we examine the corresponding S-parameters and radiation properties. All of these applications are within the strong coupling limit and, therefore, the PBG materials contain a small number of unit cells (should be thin FAL's) to satisfy compact printed design requirements. Response and scaling properties of the resulting IC's and packaged antennas are numerically examined in the microwave and millimeter-wave regimes.

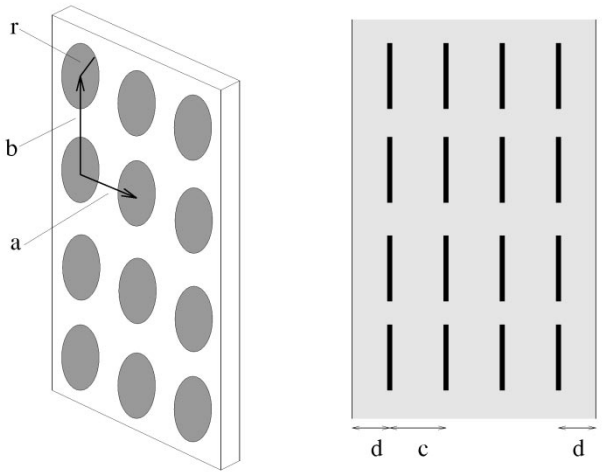

Fig. 1. PBG material made of PEC disks embedded in a dielectric host, and corresponding FSS.

II. Transfer-Matrix Analysis of PBG Materials and Scaling

Let us illustrate some of the preceding ideas by focusing on a certain PBG material composed of metalo-dielectric unit cells. We will consider an orthogonal lattice of perfect electric conductor (PEC) disks embedded in a homogeneous dielectric of real permittivity ϵ and thickness c, as shown in Fig. 1. The material will be made by stacking an arbitrary number N of such frequency-selective layers (FSL's) and will be laterally infinite, but of a finite arbitrary thickness $w = N \times c$. We will examine oblique plane-wave incidence on this material and the scaling of physical observables (reflection and transmission) relative to the parameter $k_0 \cdot c$, and compare with the well-known scaling for the corresponding dielectric slab of permittivity ϵ, which is periodic with $k_0 \cdot c$.

Consider the FSS made up by stacking N layers of the corresponding 2-D PBG medium and excited by TE plane-wave oblique incidence at angle θ. Using standard transfer-matrix theory [2], we obtain for the transmission coefficient

$$T_N \equiv \frac{R_{\text{out}}}{R_{\text{in}}} = \frac{1}{S_{11}} \tag{1}$$

where R_{in} is the initial right-going wave amplitude (with respect to the stacking direction z), and R_{out} the final right-going wave amplitude in the region past the whole structure.

The scattering matrix[1] S is given in terms of the unit-cell transfer matrix U by

$$S = T_{a,d} P_d U^N P_c^{-1} P_d T_{d,a} \tag{2}$$

where $T_{a,d}$ is the transfer matrix through an air–dielectric interface and P_c, P_d the propagation matrix through a dielectric region of thickness c and d, respectively. The unit-cell transfer matrix can be calculated to be

$$U = \frac{1}{2}\begin{pmatrix} e^{\gamma_d c}(2+Y) & e^{-\gamma_d c}Y \\ -e^{\gamma_d c}Y & e^{-\gamma_d c}(2-Y) \end{pmatrix} \tag{3}$$

where Y is the shunt admittance of one tetragonal array of disks embedded in a homogeneous dielectric.

The interface transfer matrix and propagation matrix are

$$T_{a,d} = \frac{1}{2}\begin{pmatrix} 1+\dfrac{\eta_a}{\eta_d} & 1-\dfrac{\eta_a}{\eta_d} \\ 1-\dfrac{\eta_a}{\eta_d} & 1+\dfrac{\eta_a}{\eta_d} \end{pmatrix} \quad P_c = \begin{pmatrix} e^{\gamma_d c} & 0 \\ 0 & e^{-\gamma_d c} \end{pmatrix}. \tag{4}$$

In the above, γ_i, η_i are the oblique propagation constants and wave impedances, respectively, for material $i \in \{a, d\}(a \equiv \text{air}, d \equiv \text{dielectric})$, namely,

$$\begin{aligned} \gamma_i &= jk_0 n_i \cos\theta_i \\ \eta_i &= \sqrt{\frac{\mu_0}{\epsilon_0}}\,\frac{1}{n_i \cos\theta_i} \\ \cos\theta_i &= \sqrt{1 - \frac{1}{n_i^2}\sin^2\theta} \\ n_i &= \sqrt{\epsilon_i}. \end{aligned} \tag{5}$$

Substituting for the transmission coefficient, we find (6), shown at the bottom of this page, where

$$\begin{aligned} \Psi &\equiv j\sin(k_0 cn\cos\theta_d) + \cos(k_0 cn\cos\theta_d)(Y/2) \\ \tau &\equiv \cos(k_0 cn\cos\theta_d) + \sin(k_0 cn\cos\theta_d)(jY/2) \\ \zeta &\equiv \frac{\Psi}{\tau}\sqrt{1-\left(\frac{Y}{2\Psi}\right)^2} \\ \delta &= \frac{1-\zeta}{1+\zeta}. \end{aligned} \tag{7}$$

It is important to notice that the parameter τ above characterizes the corresponding PBG material that is infinite in the z-direction ($\lim N = \infty$). This can be shown by evaluating the Floquet propagation constant along the stacking direction through the eigenvalues of the unit-cell matrix U as follows:

$$e^{-jk_F c} = \frac{\text{tr}(U)}{2} - j\sqrt{\det(U) - \left(\frac{\text{tr}(U)}{2}\right)^2}. \tag{8}$$

Given that $\det(U) = 1$, we have

$$\begin{aligned} \cos(k_F c) &= \frac{\text{tr}(U)}{2} \\ &= \cos(k_0 cn\cos\theta_d) + \sin(k_0 cn\cos\theta_d)(jY/2) \\ &\equiv \tau. \end{aligned} \tag{9}$$

We will superimpose the bandgaps obtained from (9) with the actual transmission results for thin lattices given by our explicit transmission coefficient T_N.

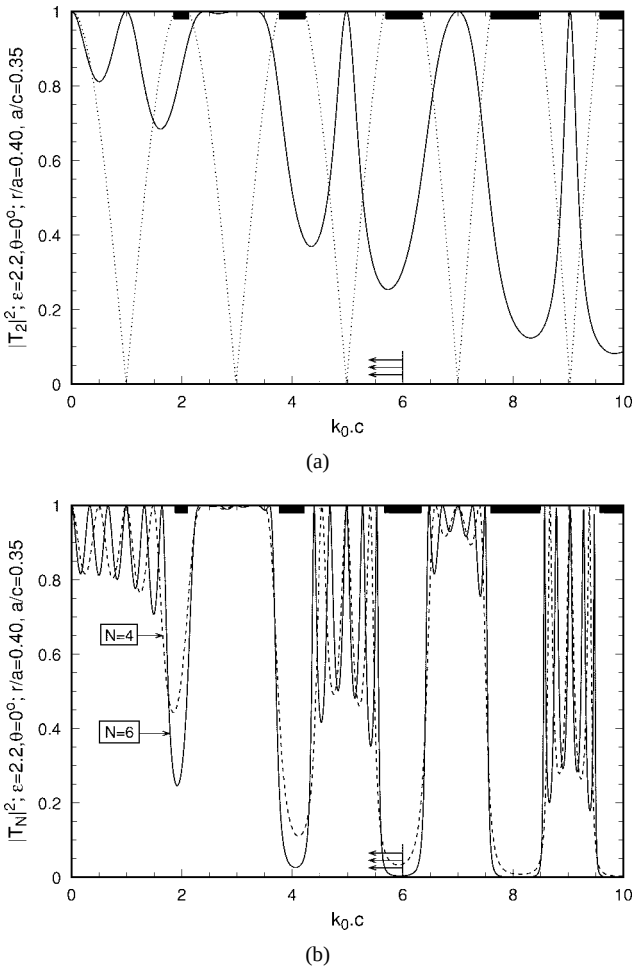

Fig. 2. (a) Normal-incidence power transmission (solid) for an FSS composed of stacking two strongly capacitive metalo-dielectric FSL's. The PBG's are also shown as the bold-line frequency regions where $|\tau| > 1$ ($|\tau|$ is plotted as the dotted curve). (b) Same as in (a), but for $N = 4$ (dashed) and $N = 6$ (solid) FSS.

[1]Unlike in transmission-line theory, the scattering matrix within the transfer-matrix formulation connects electric-field helicity amplitudes.

$$T_N = \frac{8}{[(1+\zeta)\tau]^N} \times \left\{ e^{\gamma_d(2d-c)}\left(1+\frac{\eta_a}{\eta_d}\right) \times \left(1+\frac{\eta_d}{\eta_a}\right)\left[1+\delta^N + \frac{(1-\delta^N)}{\zeta\tau}\Psi\right] + e^{-\gamma_d(2d-c)}\left(1-\frac{\eta_a}{\eta_d}\right) \times \left(1-\frac{\eta_d}{\eta_a}\right)\left[1+\delta^N - \frac{(1-\delta^N)}{\zeta\tau}\Psi\right] + \left(\frac{\eta_a}{\eta_d}-\frac{\eta_d}{\eta_a}\right)\left(1-\frac{\eta_d}{\eta_a}\right)\frac{(1-\delta^N)}{\zeta\tau}Y \right\}^{-1} \tag{6}$$

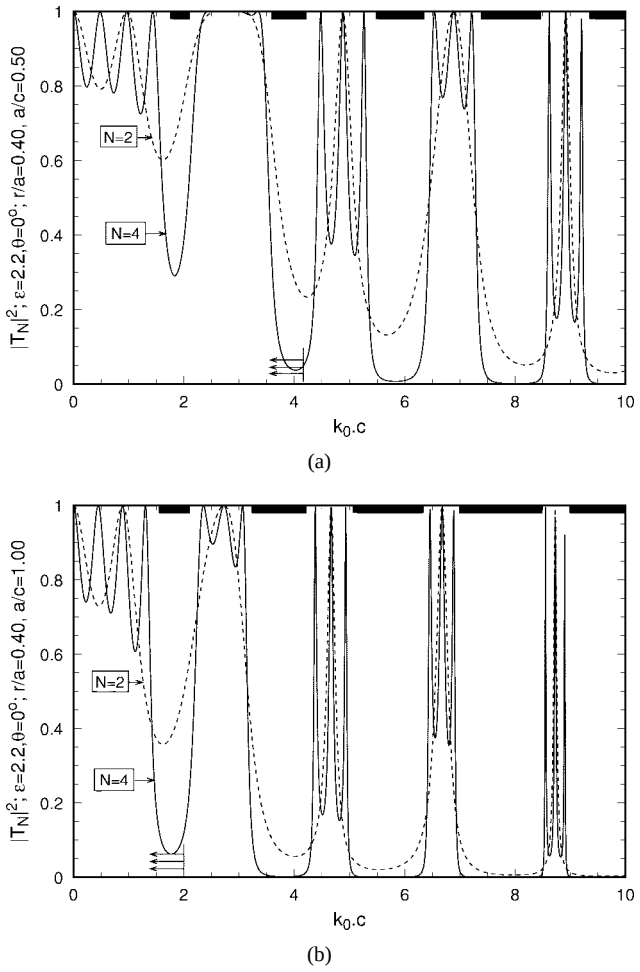

Fig. 3. Normal-incidence power transmission for N stacked FSL's and increasing capacitive interaction a/c. (a) $a/c = 0.5$. (b) $a/c = 1$.

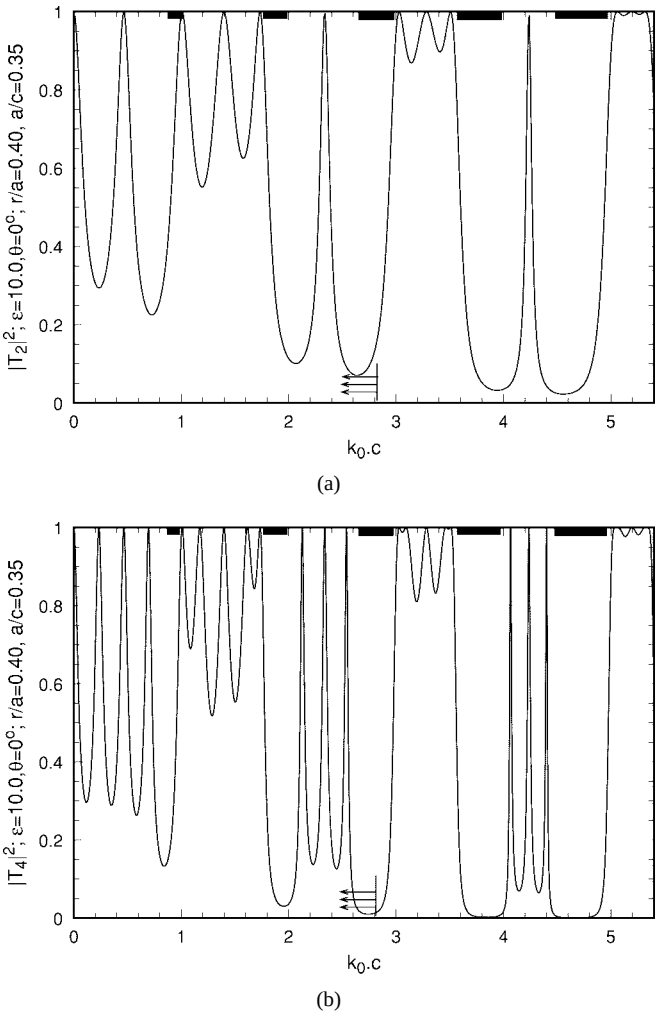

Fig. 4. Normal-incidence power transmission for an N-layer FSS and higher host permittivity. The number of PBG's scales in proportion to the host refractive index n. (a) $N = 2$. (b) $N = 4$.

For the thin-disk medium ignoring evanescent modes, the shunt admittance has been calculated analytically [3]. The result is

$$\begin{aligned} Y &= j(B_C - B_L) \\ B_C &= \frac{16}{3}\left(\frac{r}{a}\right)^3 \frac{a}{b}\frac{a}{c}\frac{nk_0c}{\cos\theta_d}\frac{1}{1-\alpha_e C_e} \\ B_L &= \frac{8}{3}\left(\frac{r}{a}\right)^3 \frac{a}{b}\frac{a}{c} nk_0c\left(\frac{1}{\cos\theta_d} - \cos\theta_d\right)\frac{1}{1-\alpha_m C_m}. \end{aligned} \quad (10)$$

The fine structure provided by the electric and magnetic polarizabilities and lattice interaction constants ($\alpha_e C_e$, $\alpha_m C_m$) can be readily calculated for a tetragonal lattice

$$\begin{aligned} \alpha_e C_e &= \frac{16}{3}\left(\frac{r}{a}\right)^3\left[\frac{1.2}{\pi}\left(\frac{a}{b}\right)^3 - 8\pi\left(\frac{a}{b}\right)^3 K_0\left(\frac{2\pi a}{b}\right)\right] \\ \alpha_m C_m &= \frac{16}{3}\left(\frac{r}{a}\right)^3\left[\frac{1.2}{2\pi}\left(\frac{a}{b}\right)^3 + \frac{1.2}{2\pi} - 4\pi\left(\frac{a}{b}\right)^3 K_0\left(\frac{2\pi a}{b}\right)\right. \\ &\qquad \left. - 4\pi K_0\left(\frac{2\pi b}{a}\right)\right] \end{aligned} \quad (11)$$

where K_0 is the modified Bessel function of the second kind. In the remainder of this section, for simplicity, we will use a square transverse lattice $a = b$, $K_0(2\pi) = 0.00\,091$ and a symmetrical FSL $2d = c$.

We derive the range of validity of the above formulas from the requirement that the leading evanescent mode propagating in the longitudinal dimension z has an amplitude that is at least as suppressed as e^{-1}. Using this criterion, we calculate the range of validity of our analytical approach as a function of dielectric refractive index, incidence angle, and longitudinal aspect ratio to be

$$k_0c \le \frac{\sqrt{\sin^2\theta + \left[\left(\frac{\pi c}{a}\right)^2 - 1\right]n^2} - \frac{\pi c}{a}\sin\theta}{n^2 - \sin^2\theta}. \quad (12)$$

In Fig. 2, we show the power transmission of a two-layer FSS under normal incidence as a function of the usual scaling variable k_0c. We observe very significant violation of the usual periodic scaling with k_0c, which characterizes the corresponding homogeneous dielectric (the latter response is simply the leftmost transmission lobe periodically repeated throughout the band, and is a Fabry–Perot resonance). We also show the formal PBG of the infinite structure obtained from the raised cosine of the Floquet propagation constant (9), namely $|\tau| > 1$. We note that the PBG's determine the

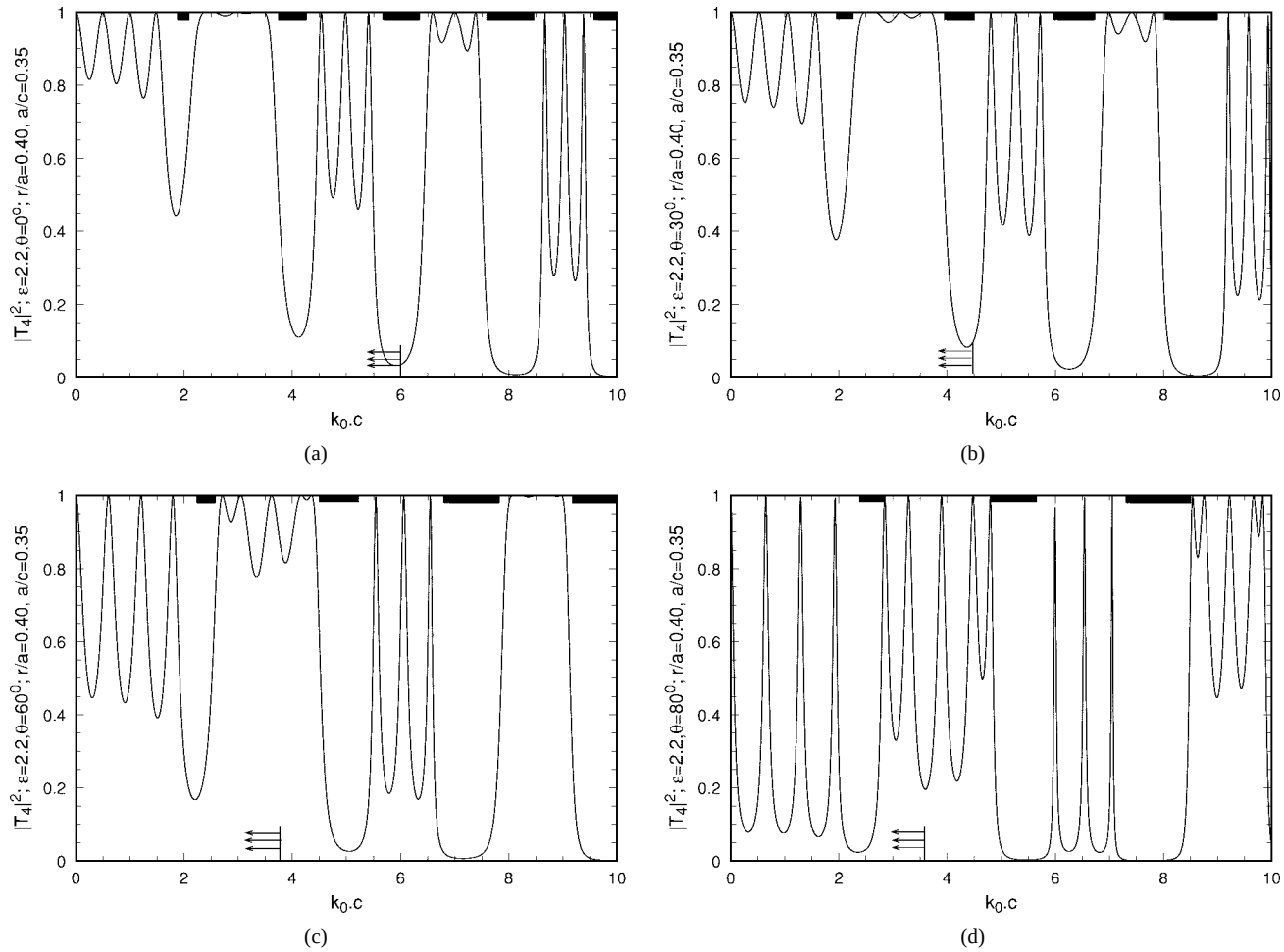

Fig. 5. TE power transmission of an $N = 4$ FSS as a function of incidence angle θ. (a) $\theta = 0°$. (b) $\theta = 30°$. (c) $\theta = 60°$. (d) $\theta = 80°$.

deep transmission stopbands, even for an FSS made as a thin lattice in the z-direction. Finally, the region to the left of the triple arrows denotes the range of validity of our analytical formulas, as given by (12). Using a modest number of FSL's, we obtain almost zero transmission stopbands, as demonstrated in Fig. 2(b).

In Fig. 3, we show the effect of increasing the capacitive interaction by increasing the longitudinal aspect ratio a/c. The transmission in the wider PBG's (larger frequencies) becomes very small for a very modest number N of FSL's.

In Fig. 4, we show the effect of increasing the host permittivity. The number of PBG's within a certain band increases in proportion to the host refractive index.

In Fig. 5, we show the angular dependence of the transmission spectrum. We observe that as the incidence angle θ increases, the PBG's (and the associated transmission stopbands for the thin lattices) widen and deepen. This presents interesting angular filtering characteristics of the FSS for specific operating frequencies.

We illustrate this issue in Fig. 6, where we show the TE transmitted power versus incidence angle for fixed frequencies chosen in the middle of the PBG's. Unlike the corresponding homogeneous dielectric, normal incidence transmission is very much suppressed, while an intermediate range of angles can have one or more passbands, including angular filtering very close to a square-pulse response. This presents interesting application possibilities for spatial filtering.

III. FE–IEM Formulation

As we saw in Section II, PBG materials are ideal candidates for FSS since the PBG's can be used to suppress or tailor-design transmission and spatial filtering above and beyond the frequency selectivity provided by multilayered homogeneous substrates. Further, frequency selectivity and scaling properties of these structures are strongly dependent on the design of the unit cell and parameters underlying the geometry of the artificial crystal. This is more so in our case, where we will focus on thin lattices for printed-circuit applications.

In order to further advance design capabilities with more complex unit cells and, most importantly, integrate these structures within realistic compact circuit architectures, numerical methods need to be used, such as volume integral equations [4], finite-element (FE) methods [5], [6], or finite difference time domain (FDTD) [7]. In [8], the combined FE method of moments (MoM) is used to treat 2-D laterally infinite periodic structures. In this paper, we present our own hybrid FE–IEM based on an evolution of the formulation by Antilla *et al.* [9] for analyzing 3-D periodic problems (with emphasis in novel FSS made up of a small number of FSL's) or for analyzing finite truncations of these structures integrated within circuits

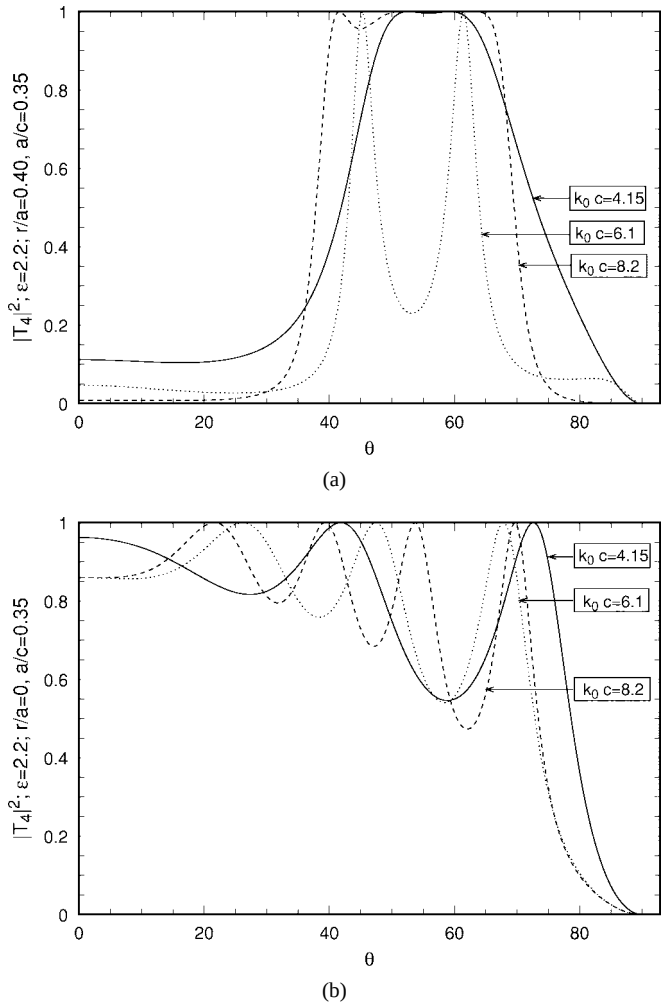

Fig. 6. (a) Space-filter response (TE power transmission versus incidence angle) of an $N = 4$ FSS for fixed frequencies in the bandgaps. (b) Same as in (a) for the corresponding homogeneous dielectric with the disks removed ($r = 0$).

or packaged antennas. We have tested and validated our hybrid code in specific geometries against published results [10], [11] with excellent agreement. This code has the capability of synthesizing FSS by stacking FSL's rotated with respect to each other, resulting in extra frequency-selectivity flexibility. Further, it can handle arbitrary curvilinear unit cells and conformal lattices once we implement a curvilinear mesh generator.[2]

A. FE-Method Formulation

The FE method for the electric-field formulation uses linear vector-edge-based expansion on super parametric hexahedral elements (curvilinear bricks). The use of edge-based field unknowns removes the problem of spurious solutions which occur for node-based fields through over-specification of the normal field components across material interfaces. These edge-based fields guarantee the matching of tangential fields across material interfaces, and allow the easy implementation of boundary conditions on perfect-conducting boundaries.

[2]Implementation of the curvilinear mesh generator will be accomplished in the near future.

The equation valid in the interior regions, which is discretized by the FE method is

$$\int\int\int_V \left[\frac{1}{\mu_r^*}\nabla\times\vec{E}\cdot\nabla\times\vec{W} - k_0^2\epsilon_r^*\vec{W}\cdot\vec{E}\right]dv - \int\int_s \vec{W}\cdot\left[jk_0Z_0\left(\hat{n}\times\vec{H}\right)\right]\mathrm{ds} = 0 \quad (13)$$

where $\vec{W}$ represents vector test functions of the same form as $\vec{E}$ and satisfy the same boundary conditions, and ϵ_r^* and μ_r^* can have arbitrary complex values within each element. This equation results from applying the method of weighted residuals to the vector-wave equation valid in the interior region, and using the divergence theorem to transfer one differentiation onto the weight function. Choosing $\vec{W}$ to have the same form as $\vec{E}$ yields Galerkin's approach, which is exactly equivalent to applying the Rayleigh–Ritz method to the variational functional of the original equation. Using this equation allows the relaxation of continuity requirements on the $\vec{E}$ field to a continuous approximation, provided that $\vec{W}$ is also a continuous approximation. The resulting integration is well behaved, and since no Green's function is present, the interactions are local, resulting in a sparse matrix upon discretization. The source couples into the volume through the $\vec{H}$ field on the boundary. This can be either a feed aperture for a microstrip-circuit configuration, or the outer surface for scattering problems among a variety of model problems.

For closed cavities or shielded structures, the surface integral in (13) vanishes and the resulting system of homogeneous equations can be solved for the eigenvalues k_0 of the resonant cavity. The elements have nonorthogonal coordinates, so the field unknowns are expressed as covariant projections, and all vector operations are performed in generalized coordinates. Special elements, which correctly model field singularities near edges and corners, can be easily incorporated to improve convergence.

B. IEM Formulation

The integral equation is formulated for either the half-space dyadic Green's function or the free-space dyadic Green's function, so that a wide range of geometries can be handled. For the half-space Green's function, the magnetic-field formulation (MFIE) is chosen so that when the surface becomes flush with the ground plane, the incident field does not vanish. The MFIE has the form

$$\hat{n}\times\vec{H}^i\left(\vec{R}\right) = \frac{\vec{J}\left(\vec{R}\right)}{2} - \int\int_{s'}\hat{n}\times\left[\nabla\times\overline{\overline{G}}_1\left(\vec{R},\vec{R}'\right)\cdot\vec{J}\left(\vec{R}'\right)\right]\mathrm{ds}' + jk_0Y_0\hat{n}\times\int\int_{s'}\overline{\overline{G}}_2\left(\vec{R},\vec{R}'\right)\cdot\vec{M}\left(\vec{R}'\right)\mathrm{ds}' \quad (14)$$

where

$$\overline{\overline{G}}_2\left(\vec{R},\vec{R}'\right) = \left(\overline{\overline{I}} - \frac{\nabla\nabla'}{k_0^2}\right)\left[g\left(\vec{R},\vec{R}'\right) + g\left(\vec{R},\vec{R}_i'\right)\right] - 2\hat{z}\hat{z}g\left(\vec{R},\vec{R}_i'\right) \quad (15)$$

$$\nabla \times \overline{\overline{G}}_1\left(\vec{R}, \vec{R}'\right) = \left[\nabla g\left(\vec{R}, \vec{R}'\right) \times \overline{\overline{I}} - \nabla g\left(\vec{R}, \vec{R}_i'\right) \times \overline{\overline{I}}_i\right] \tag{16}$$

$$g\left(\vec{R}, \vec{R}'\right) = \frac{e^{-jk_0|\vec{R}-\vec{R}'|}}{4\pi\left|\vec{R}-\vec{R}'\right|} \tag{17}$$

$\vec{M}(\vec{R}')$ is the magnetic current, and the image point $\vec{R}_i$ has the $\hat{z}$ component sign reversed. The free-space version has the image components removed.

The MFIE is discretized using the Galerkin version of the method of weighted residuals similar to the FE method by choosing test functions to be the same piecewise linear functions that are used for field expansions. This approach can handle the higher order singularity introduced by the $\nabla\nabla g$ term in (15) by using integration by parts twice. The remaining integrals are well behaved and are evaluated numerically after the static singularity in g has been extracted and computed analytically. The presence of the Green's function results in a dense matrix after discretization.

For laterally periodic FSS, we can make use of Floquet's boundary conditions on the surface surrounding the unit cell, and reduce the MFIE into a spatial-periodic form

$$\begin{aligned}\iint_s \vec{W}\left(\vec{R}\right) \cdot \left[\hat{n} \times \vec{H}^i\left(\vec{R}\right)\right] \mathrm{ds} &= \iint_s \vec{W}\left(\vec{R}\right) \cdot \left[\hat{n} \times \vec{H}\left(\vec{R}\right)\right]/2 \,\mathrm{ds} + jk_0 Y_0 \iint_s \vec{W}\left(\vec{R}\right) \\ &\times \hat{n} \times \iint_{s'} g_p\left(\vec{R}, \vec{R}'\right) \vec{M}\left(\vec{R}'\right) \mathrm{ds}' \,\mathrm{ds} - 1/(jk_0 Z_0) \\ &\times \iint_s \vec{W}\left(\vec{R}\right) \hat{n} \times \nabla\nabla \cdot \iint_{s'} g_p\left(\vec{R}, \vec{R}'\right) \vec{M}\left(\vec{R}'\right) \mathrm{ds}' \,\mathrm{ds}.\end{aligned} \tag{18}$$

Here, g_p is the spatial periodic Green's function

$$g_p = \sum_{m=-\infty}^{+\infty} \sum_{n=-\infty}^{+\infty} e^{-jk_0 R_p}/(4\pi R_p) e^{-jk_{0x} ma - jk_{0y} nb}. \tag{19}$$

By applying Poisson's summation formula twice, the last two terms in (18) can be cast into the form

$$\begin{aligned}jk_0 Y_0 \iint_s \vec{W}\left(\vec{R}\right) \cdot \hat{n} \times \iint_{s'} \widetilde{g}_p\left(\vec{R}, \vec{R}'\right) \\ \times \vec{M}\left(\vec{R}'\right) \mathrm{ds}' \,\mathrm{ds} - 1/(jk_0 Z_0) \iint_s \vec{W}\left(\vec{R}\right) \hat{n} \\ \times \nabla\nabla \cdot \iint_{s'} \widetilde{g}_p\left(\vec{R}, \vec{R}'\right) \vec{M}\left(\vec{R}'\right) \mathrm{ds}' \,\mathrm{ds}\end{aligned} \tag{20}$$

where

$$\begin{aligned}\widetilde{g}_p\left(\vec{R}, \vec{R}'\right) = 1/(2ab) \sum_{m=-\infty}^{+\infty} \sum_{n=-\infty}^{+\infty} \\ \times e^{-j\beta_{xm}(x-x') - j\beta_{yn}(y-y') - j\beta_{zmn}(z-z')}/(j\beta_{zmn})\end{aligned} \tag{21}$$

and β_{xm}, β_{yn}, and β_{zmn} are the propagation constants of the corresponding mnth space harmonic in three directions, respectively.

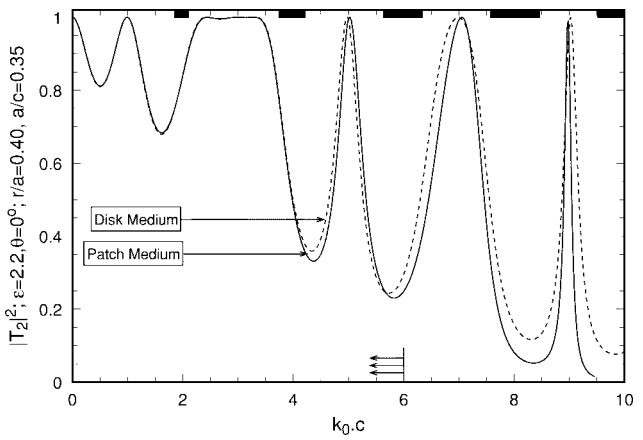

Fig. 7. Normal-incidence power transmission for a two-layer disk medium (treated analytically) and the equivalent patch medium (treated with our FE–IEM code).

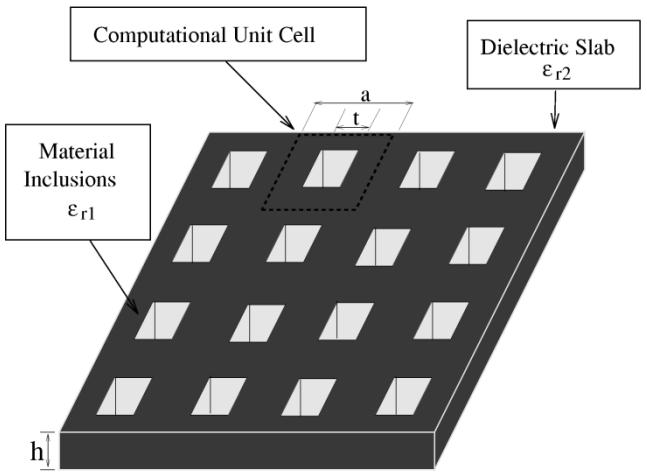

(a)

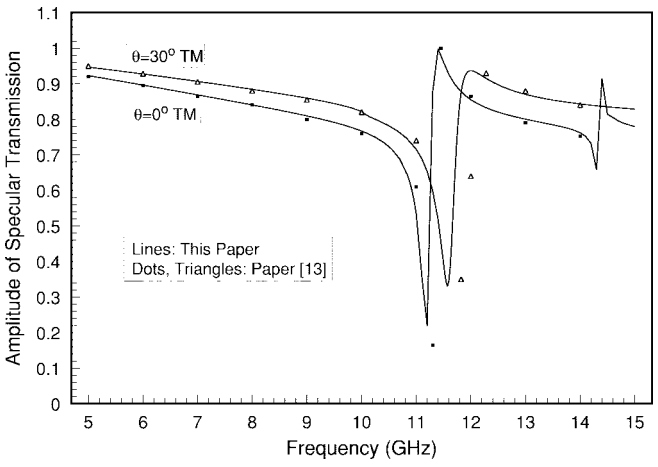

(b)

Fig. 8. (a) One layer of high-contrast dielectric FSL. (b) TM amplitude transmission.

The combined matrix system from the FE–IEM is solved via a sparse solver, and the frequency-selective characteristics are calculated through a post-processing code.

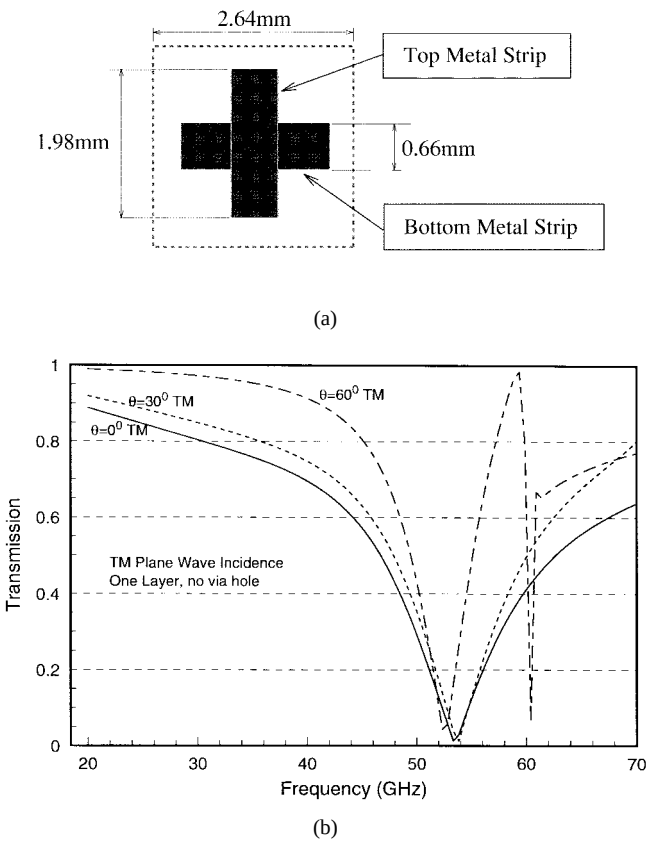

Fig. 9. (a) One layer of capacitive-inductive metalo-dielectric unit cells. The substrate has $\epsilon = 2.2$ and thickness $c = 0.787$ mm. (b) TM amplitude transmission.

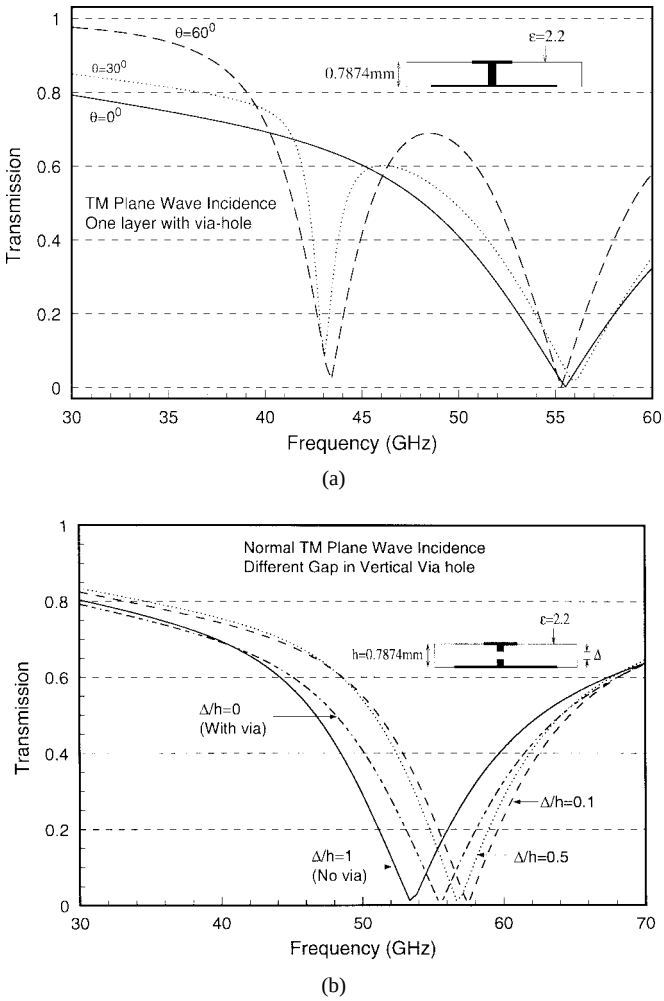

Fig. 10. (a) TM amplitude transmission for an FSL of strongly capacitive-inductive metalo-dielectric unit cells with vias. (b) Same as in (a), with tunable vias through a gap.

IV. Design and Optimization of FSS's

In this section, we provide several results of our FE–IEM code for FSS's. We will focus mostly on metalo-dielectric unit cells with strongly capacitive interactions.

In Fig. 7, we compare the FSS, made up of circular PEC disks and solved analytically in Section II with a medium of square PEC patches implanted on the same lattice and analyzed by our FE–IEM code. We note that our code cannot yet handle curvilinear geometries, therefore, the implants are square PEC patches rather than circular disks. Therefore, in Fig. 7, we compare the two media where the patch side d is chosen by the equivalent aperture formula [12]

$$\frac{d}{a} = \left(\frac{32}{3\pi}\right)^{1/3} \frac{r}{a}. \tag{22}$$

We see that, within the range of validity of our analytical treatment (to the left of the triple arrows), the results are in *excellent agreement.* This impressive agreement at once validates both our analytical formulas *and* our FE–IEM code.

Outside the validity range $k_0 c \geq 6$, (12), Fig. 7 shows that our analytical treatment still provides very useful and fast (10^3 points/s) insights concerning all aspects of material parameter optimization. In that region, only our FE–IEM results should be trusted, but the analytical response is still quite close to the FE–IEM results. Further, the large transmission stopbands fall accurately within the PBG obtained from (9), denoted by the boldface lines on the top of the figure. In future work, we will pursue further the differences in implant geometry, including derivation of polarizabilities for orthogonal and ellipsoidal shapes on one hand and a curvilinear mesh generator on the other.

We have further analyzed several designs of 2-D artificial media implanted periodically with a variety of scatterers. Given that we require thin and laterally compact geometries, our FE–IEM code is ideal in analyzing integration of finite thin lattices of these materials within the general packaged architectures we are concerned with.

To further validate our FE–IEM code, we show in Fig. 8 a single FSL containing high-contrast dielectric square inclusions perforating the host medium all the way. We observe the transmission stopband, which moves in frequency with changing incidence angle. These results are in excellent agreement with the ones published in the literature [13]. If the inclusions are substituted with metal, the stopband is locked in frequency for all angles.

In Figs. 9–13, we explore more complicated metalo-dielectric FSL's, including tunable designs and the effects on transmission of stacking them in various ways.

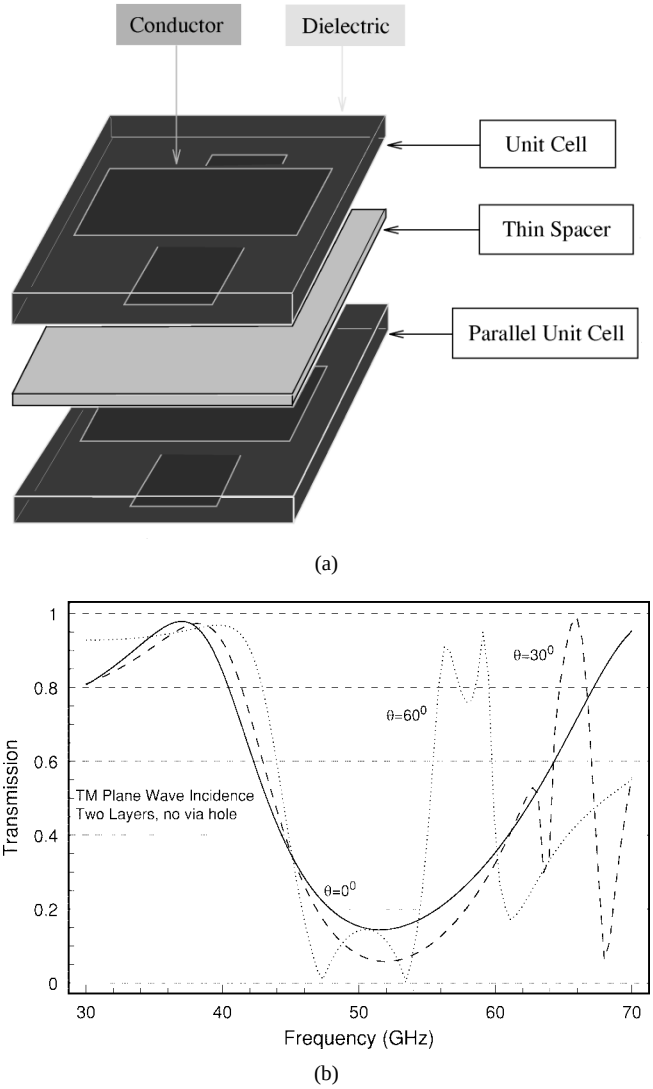

Fig. 11. (a) Thin lattice formation for FSS's. Parallel stacking of capacitive-inductive FSL's. (b) TM amplitude transmission.

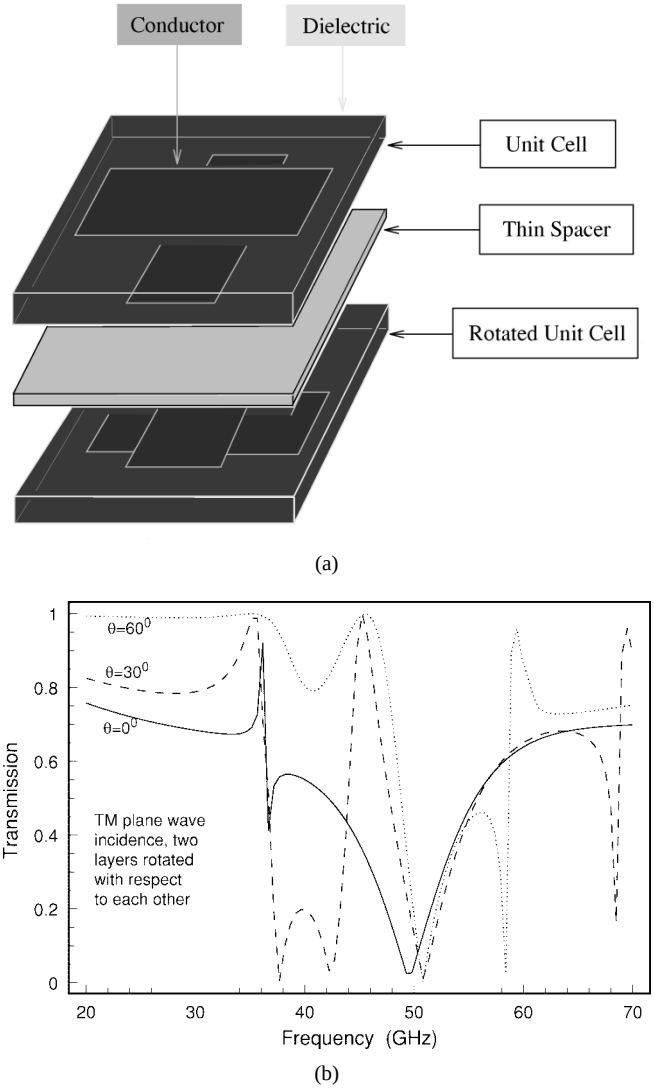

Fig. 12. (a) Thin lattice formation for FSS's. 90°-rotated stacking of capacitive-inductive FSL's. (b) TM amplitude transmission.

In Fig. 9, we explore a metalo-dielectric unit cell having both strong capacitive and inductive interactions. In Fig. 10, in particular, we show the transmission characteristics of an FSL produced by capacitive unit cells with tunable conducting vias. Varying the via gap dimension tunes the transmission stopband within a good-size bandwidth. Equivalent results can be obtained using biasable ferroelectric or ferromagnetic materials instead of the via gap, which allows for tuning the structure externally. In Figs. 11 and 12, we explore two extreme cases of stacking two such FSL's together: parallel and 90°-rotated, respectively. We observe that, in the former case, a transmission stopband develops, which is angle-independent. In the latter case, the stopband only blocks intermediate angles.

This response becomes cleaner if unit cells with vias are stacked, as in Fig. 13, where we obtain a narrow-band direction-selective stopband and a broader direction-independent stopband. It is clear that these designs can be further tailored and tuned with an appropriate parameter search.

V. Integration of Thin Artificial Lattices Within IC and PCA Architectures

In this section, we analyze the integration of some of the previous FSS designs within realistic thin compact printed circuit and packaged antenna architectures. For all these applications, in order to obtain PBG effects of the type discussed in Section II, the unit-cell size should be comparable to the operating wavelength. Otherwise, the artificial medium will be electrically equivalent to a uniform dielectric with, at most, a dispersive behavior. On the other hand, due to the realistic limitation of compact lateral size, few unit cells can be included, and the system reacts, in principle, differently than its infinite PBG counterpart.

We first present our results for integration of thin FAL's into IC architectures at high frequencies. The structures under analysis are shown in Figs. 14(a) and 15(a). A combined 2-D/3-D FE method is used to analyze such classes of structures. The 2-D FEM is used to get the modal distribution, characteristic impedance, and propagation constant of the uniform transmission line, which is used later in the 3-D FEM

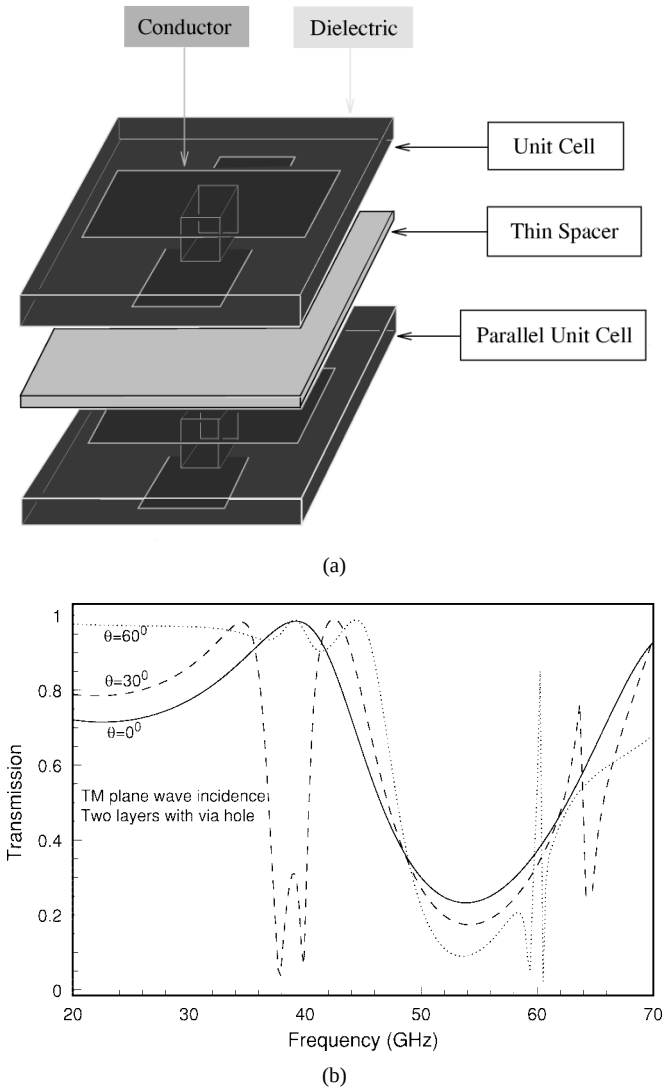

Fig. 13. (a) Thin lattice Formation for FSS's. Parallel stacking of tunable capacitive-inductive FSL's. (b) TM amplitude transmission.

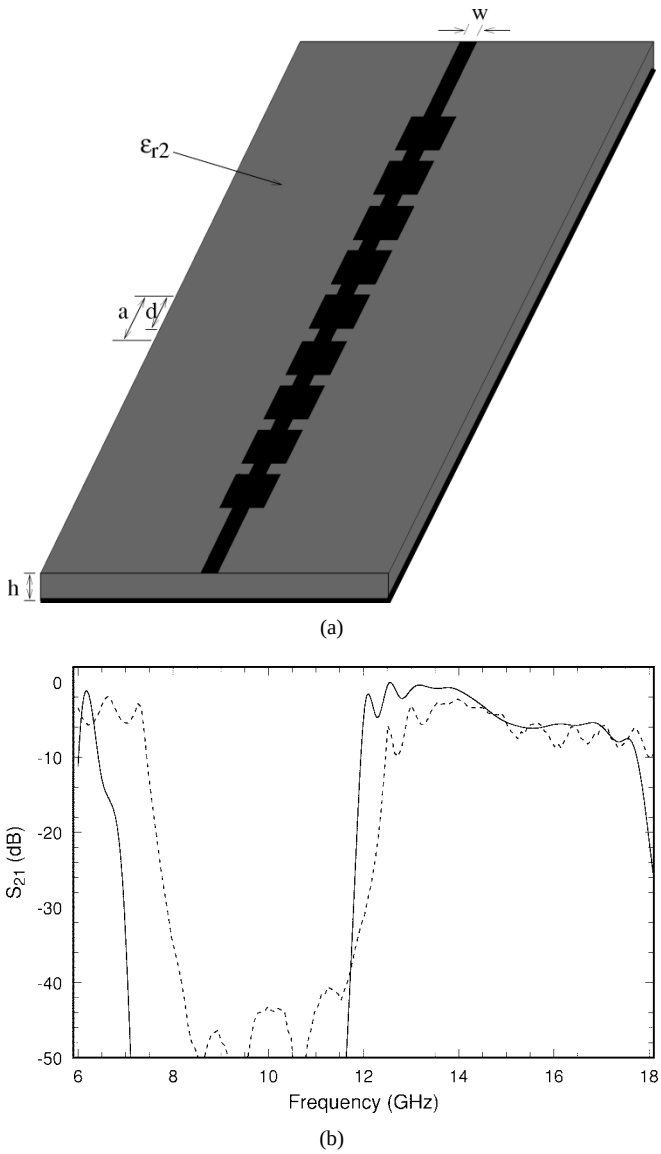

Fig. 14. (a) Printed microstrip line on a single row of periodically printed PEC patches. $a = 5.08$ mm, $d = 2.54$ mm, $w = 0.686$ mm, $h = 0.635$ mm, $\epsilon_{r2} = 10.5$. (b) Transmission calculated (solid) and measured (dashed) in the region of the first bandgap.

analysis of the whole circuitry. This method has been presented in [14] for general monolithic microwave integrated circuits (MMIC's), while we now use it for circuits with thin FAL materials.

Fig. 14(a) is a printed microstrip periodic filter, which we have also fabricated and measured. Fig. 14(b) shows the transmission, both calculated (solid) and measured (dashed). The shape and bandwidth of the measured bandgap agrees with the simulated one, up to the noise level of the network analyzer. The position of the measured bandgap is slightly shifted relative to the theoretical one, probably due to uncertainties in the substrate permittivity.

Fig. 15(a) shows a perforated geometry with three rows of holes. The simulated data is presented in Fig. 15(b). *An extremely large bandgap* of more than 80 dB has been found near 14 GHz for S_{21}. A similar result was obtained experimentally for a slightly different geometry [15]. Notice again that existence of this bandgap strongly violates the usual scaling with frequency, as expected for homogeneous substrates.

For printed microstrip antennas, it has been shown that substantial directive gain enhancement may be achieved, with the use of multiple substrates [16] or with one single PBG layer [17]. In the latter case, a gain enhancement of 14.5 dB was found for an elementary printed dipole. Motivated by this result, we examine the important issue of using PBG substrates/covers within the target framework of practical laterally finite compact semiclosed PCA's. Since the resulting thin FAL may have a very different response from their laterally infinite counterparts, the issue of obtaining similar directive gains for compact PCA's is an important one. In this paper, we will only present results for PBG covers.

In Figs. 16 and 17, we present a thin-FAL-covered (packaged) patch antenna printed on a homogeneous substrate, the whole system enclosed within a compact cavity and fed by a current probe. The overall size is set by the requirement that the cover contains few unit cells, each of the order of a half-

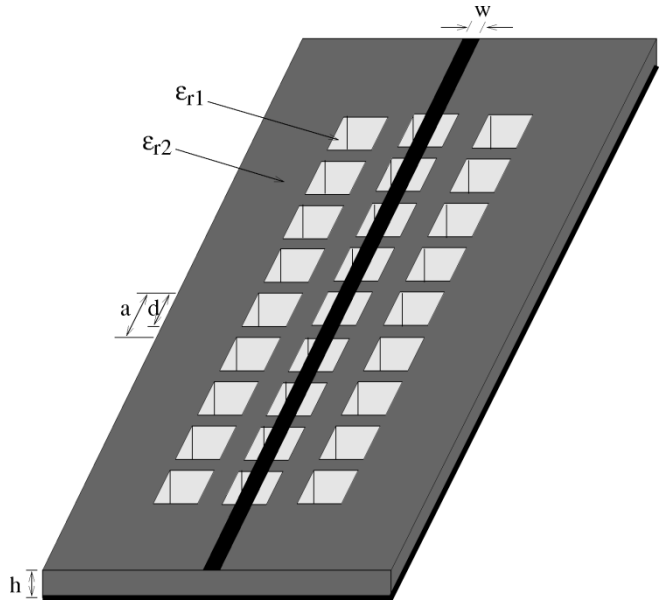

(a)

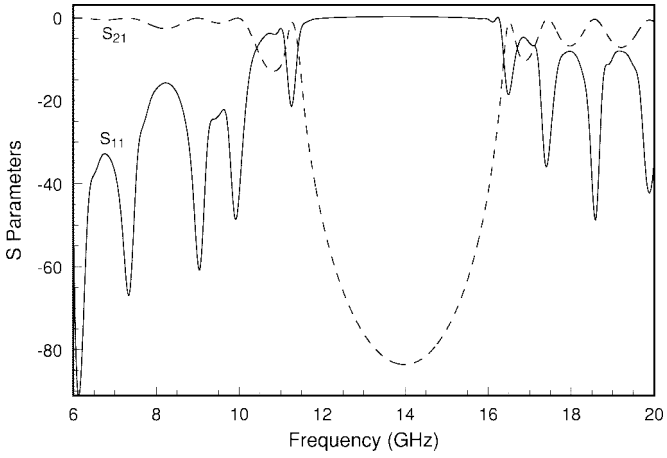

(b)

Fig. 15. (a) Printed microstrip line on a high-contrast dielectric thin FAL substrate. (b) Scattering parameters (in decibels) for a printed microstrip line on a high-contrast thin FAL substrate. $a = 5.08$ mm, $d = 2.54$ mm, $w = 0.686$ mm, $h = 0.635$ mm, $\epsilon_{r1} = 1.0$, and $\epsilon_{r2} = 10.5$.

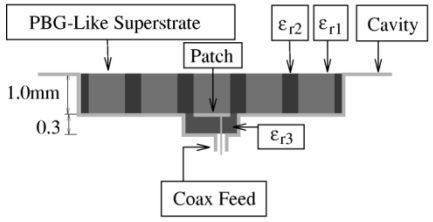

(a)

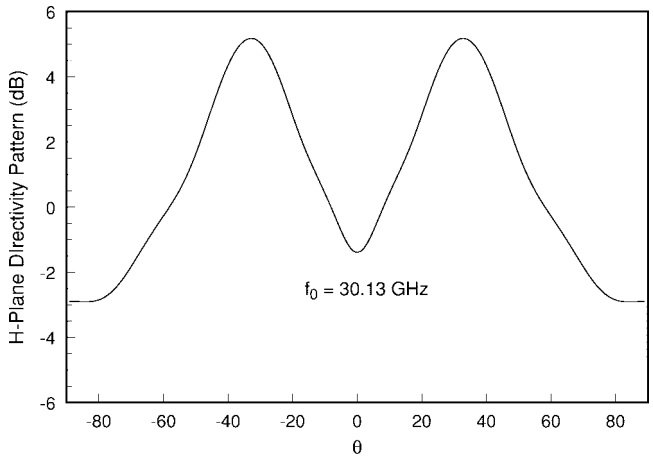

(b)

Fig. 16. (a) Cavity-backed multimode patch antenna printed on a homogeneous substrate and covered by a high-contrast dielectric FAL (5×5) unit cells. Patch size $= 5 \times 5$ mm, $\epsilon_{r2} = 10$, $\epsilon_{r1} = 1$, $\epsilon_{r3} = 2.2$, unit-cell size $= 5 \times 5$ mm, air-block size $= 3 \times 3$ mm. (b) Double-beam H-plane radiation pattern.

wavelength (volumetric average) at a target wavelength. This is a multimode antenna with enhanced directivity capabilities. For a 5×5 unit-cell cover, we can have a double-beam pattern, shown in Fig. 16(b). Single-beam patterns with very high directive gain of 10 dB are possible, as shown in Fig. 17(b). We have also found that by using a 7×7 unit-cell cover, a similar pattern with that of Fig. 17(b) is obtained, with peak directivity of 12 dB. We thus see that, with appropriate design, thin FAL substrates or covers can be used in integrated compact geometries with results similar to their laterally infinite counterparts.

VI. Conclusions

In this paper, we have presented a general analysis of thin artificial lattices and PBG materials based on an analytical approach as well as on our hybrid FE–IEM approach. We have examined a variety of material designs for freestanding FSS applications, as well as integration of thin FAL's of these materials within IC and packaged printed antenna architectures.

In a variety of cases, we have demonstrated that PBG's characterizing these materials create frequency-scaling violations for the corresponding circuits, and have provided a full-wave analysis for a variety of designs.

For FSS, we have obtained metallo-dielectric thin artificial lattices with tailor-designed transmission stopbands and spatial filtering properties with respect to incident angle.

For microstrip circuit applications, we have demonstrated that nonscalable extremely high transmission suppression (>80 dB) is possible by using high-contrast permittivity dielectric thin FAL's with tailor-designed PBG's in the microwave or millimeter-wave regime.

Finally, we have integrated high-contrast permittivity dielectric thin FAL's within semiopen or covered (packaged) PCA's. We find designs with multimode capabilities and very high single-beam directivity gains.

In the near future, we will present work focusing on each of the general aspects presented here: further analytical work in modeling thin FAL as FSS based on our transfer-matrix approach in conjunction with our FE–IEM code. This will include Cartesian implant geometries and curvilinear mesh generation, respectively, with the final objective of providing accurate scattering/circuit equivalents to the computationally demanding FE–IEM code, which will provide the basis for

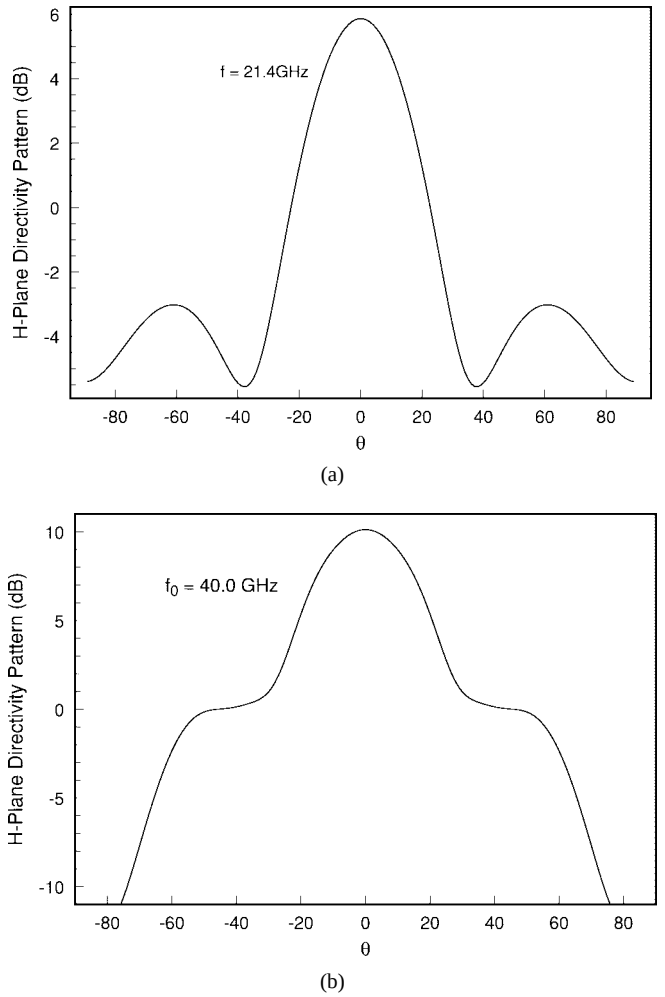

Fig. 17. (a) High-gain single-beam H-plane radiation pattern (5×5). (b) Highest gain single-beam H-plane radiation pattern (5×5).

high-speed low-memory future coding for millimeter-wave applications. Second, a variety of optimized designs with new conformal topologies, including curvilinear ones, for thin FAL, applied to FSS's, microwave integrated circuits (MIC's) and MMIC's printed on these materials. Finally, optimized compact packaged PCA printed on or covered with various dielectric or metalo-dielectric thin FAL's will be provided for a variety of pattern-shaping or directivity-enhancement applications.

ACKNOWLEDGMENT

The authors wish to thank Dr. C. Kyriazidou for assistance with the layout and fabrication and R. Ramirez for corroborating our microstrip simulations with the ALFIOS MoM code.

REFERENCES

[1] E. Yablonovitch, "Photonic band-gap structures," *J. Opt. Soc. Amer.*, vol. 10, no. 2, p. 283, 1993.

[2] M. Born and E. Wolf, *Principles of Optics*, 4th ed. New York: Pergamon, 1970, pp. 66–70.

[3] R. E. Collin, *Field Theory of Guided Waves*, 2nd ed. Piscataway, NJ: IEEE Press, 1991, pp. 771–772.

[4] H. Y. Yang, "Characteristics of guided and leaky waves on multilayer thin-film structures with planar material gratings," *IEEE Trans. Microwave Theory Tech.*, vol. 45, pp. 428–435, Mar. 1997.

[5] R. Coccioli, T. Itoh, and G. Pelosi, "A finite element-generalized network analysis of finite thickness photonic crystals," in *IEEE MTT-S Symp. Dig.*, Denver, CO, June 1997, pp. 195–198.

[6] E. W. Lucas and T. P. Fontana, "A 3-D hybrid finite element/boundary element method for the unified radiation and scattering analysis of general infinite periodic arrays," *IEEE Trans. Antennas Propagat.*, vol. 43, pp 145–153, Feb. 1995.

[7] D. Sievenpiper *et al.*, "3D metallo-dielectric photonic crystals with strong capacitive coupling between metallic islands," *Phys. Rev. Lett.*, submitted for publication.

[8] S. D. Gedney, J. F. Lee, and R. Mittra, "A combined FEM/MoM approach to analyze the plane wave diffraction by arbitrary gratings," *IEEE Trans. Antennas Propagat.*, vol. 40, pp. 363–370, Feb. 1992.

[9] G. Antilla and N. G. Alexopoulos, "Scattering from complex three-dimensional geometries by a curvilinear hybrid finite-element-integral equation approach," *J. Opt. Soc. Amer. A, Opt. Image Sci.* vol. 11, no. 4, pp. 1445–1457, Apr. 1994.

[10] J. Jin and J. L. Volakis, "A hybrid finite element method for scattering and radiation by microstrip patch antennas and arrays residing in a cavity," *IEEE Trans. Antennas Propagat.*, vol. 39, pp. 1598–1604, Nov. 1991.

[11] J. L. Volakis, T. Ozdemir, and J. Gong, "Hybrid finite-element methodologies for antennas and scattering," *IEEE Trans. Antennas Propagat.*, vol. 45, pp. 493–507, Mar. 1997.

[12] C. G. Montgomery, R. H. Dicke, and E. M. Purcell, *Principles of Microwave Circuits* (MIT Radiation Laboratory Series 8). New York: McGraw-Hill, 1948.

[13] H. Y. Yang, R. Diaz, and N. G. Alexopoulos, "Reflection and transmission of waves from multilayer structures with planar-implanted periodic material blocks," *J. Opt. Soc. Amer. B, Opt. Phys.*, vol. 14, pp. 2513–2521, Oct. 1997.

[14] A. Polycarpou, P. Tirkas, and C. Balanis, "The finite-element method for modeling circuits and interconnects for electronic packaging," *IEEE Trans. Microwave Theory Tech.*, vol. 45, pp. 1868–1874, Oct. 1997.

[15] V. Radisic, Y. Qian, R. Coccioli, and T. Itoh, "Novel 2-D photonic bandgap structure for microstrip lines," *IEEE Microwave Guided Wave Lett.*, vol. 8, pp. 69–71, Feb. 1998.

[16] H. Y. Yang and N. G. Alexopoulos, "Gain enhancement methods for printed circuit antennas," *IEEE Trans. Antennas Propagat.*, vol. AP-35, pp. 860–863, July 1987.

[17] H. Y. Yang, N. G. Alexopoulos, and E. Yablonovitch, "Photonic bandgap materials for high-gain printed circuit antennas," *IEEE Trans. Antennas Propagat.*, vol. 45, pp. 185–186, Jan. 1997.

Harry Contopanagos (M'98) received the B.S. degree in physics from the National University of Athens, Athens, Greece, in 1984, and the M.S. and Ph.D. degrees in physics from the University of Michigan at Ann Arbor, in 1989 and 1991, respectively.

From 1991 to 1993, he worked as a Research Associate at the Institute for Theoretical Physics, State University of New York at Stony Brook, where he performed research on scattering theory in quantum electrodynamics and quantum chromodynamics. From 1993 to 1996, he worked as a Research Associate at the High Energy Physics Division, Argonne National Laboratory, where he provided theoretical predictions for the production cross section of the newly discovered Top-Quark, which were in excellent agreement with subsequent experiments. Since 1997, he has been with the Electrical Engineering Department, University of California at Los Angeles (UCLA), where he works on theory and fabrication of composite electromagnetic media, applications in compact high-frequency waveguide filters, printed antennas, and physical modeling of communication channels. He has authored ten technical publications in the area of electromagnetics and 30 publications in the area of high-energy physics.

Lijun Zhang was born in Hubei, China, in 1973. He received the B.S. and M.S. degrees from the University of Science and Technology of China, Hefei, China, in 1993 and 1996, respectively, and is currently working toward the Ph.D. degree at the University of California at Los Angeles.

His current research activities include both the numerical modeling of PBG materials and their application in printed-circuit and antenna environment.

Nicolaos G. Alexopoulos (S'68–M'69–SM'82–F'87) was born in Athens, Greece, on April 14, 1942. He graduated from the Eighth Gymnasium of Athens, Athens, Greece in 1959, and received the B.S.E.E., M.S.E.E., and Ph.D. degrees from the University of Michigan at Ann Arbor, in 1965, 1967, and 1968, respectively.

He joined the School of Engineering and Applied Science, University of California at Los Angeles (UCLA) where he was a member of the faculty of the Electrical Engineering Department from 1969 to 1996. While at UCLA, he served as Associate Dean for Faculty Affairs from 1986 to 1987, and Chair of the Electrical Engineering Department from 1987 to 1992. Since January 1997, he has been a Professor in the Electrical and Computer Engineering Department, University of California at Irvine, where he also serves as the Dean of the School of Engineering. He has served over the years as a Consultant to a variety of U.S. and foreign corporations and the U.S. Government. He has authored over 250 refereed journal and conference proceedings papers. His recent research activities have focused on the modeling and design of 3-D IC's and printed antennas in multilayered materials, wireless communication antennas and systems, interconnect problems in complex networks, novel materials and smart structures in low observable systems, and computational methods. He has also been on the editorial board of various professional journals and, more recently, served as Editor-in-Chief of *Electromagnetics.*

Dr. Alexopoulos was co-recipient of the IEEE S. E. Schelkunoff Prize Best Paper Award in 1985 and 1998.